Modeling of Evaporation from Nanopores with Nonequilibrium and Nonlocal Effects

Modeling of evaporation from nanopores with non-equilibrium and non-local effects

Zhengmao Lu, Shankar Narayanan and Evelyn N. Wang[*]

Department of Mechanical Engineering, Massachusetts Institute of Technology, Cambridge, Massachusetts 02139, USA

Evaporation from nanopores is of fundamental interest in nature and various industrial applications. We present a theoretical framework to elucidate evaporation and transport within nanopores by incorporating non-equilibrium effects due to the deviation from classical kinetic theory. Additionally, we include the non-local effects arising from phase-change in nanoporous geometries, and the self-regulation of the shape and position of the liquid-vapor interface in response to different operating conditions. We then study the effects of different working parameters to determine conditions suitable for maximizing evaporation from nanopores.

I. Introduction

Evaporation from micro/nano structures is a ubiquitous phenomenon which plays an important role in nature and industrial applications, such as transpiration in plants [1], mammalian perspiration [2], electronic cooling [3, 4, 5, 6, 7, 8] and water desalination [9, 10]. A fundamental understanding of interfacial transport at the nanoscale is necessary to take advantage of phase change in such structures, among which nanopores have been of particular interest (Figure 1 (a)) [3, 4, 5, 6, 7, 8, 10]. Consequently, there have been several efforts to analyze evaporation in nanopores (~10 - 100 nm

[*] To whom correspondence should be addressed: enwang@mit.edu

in diameter) [11, 12, 13, 14], where the liquid flow was modeled using the Navier-Stokes equation, the interface was characterized with the augmented Young-Laplace equation [15], and the interfacial heat/mass flux was described using the Schrage equation derived from kinetic theory [16]. However, this approach to evaluate the interfacial flux is generally not applicable for several reasons. While the traditional approach to evaluate interfacial mass flux accounts for mass conservation, it does not consider momentum balance and energy conservation [17], which results in over prediction of the interfacial flux, especially at higher evaporation rates [18]. Consequently, the traditional approach cannot incorporate the non-equilibrium effects close to the liquid-vapor interface during intense evaporation [18, 19, 20]. A continuum approach to analyze the vapor flow in the nanopore is also inaccurate since the pore size is either comparable or smaller than the mean free path of the vapor molecules [21, 22]. More interestingly, due to the large curvature of the interface in the nanopore, and the possibility of emitted vapor molecules condensing back onto the interface, the net interfacial flux at any given location may be influenced by evaporation in the surrounding regions in the same pore. Consequently, since the interfacial flux at a given location cannot be calculated simply as an explicit function of the local temperature and pressure, evaporation from the nanopores is not a locally expressible phenomenon, as modeled traditionally [11, 12, 13, 14]. Furthermore, in the case of nanoporous membranes, evaporation from a single pore may also be influenced by neighboring pores, since vapor originating from adjacent pores can move laterally and interact with each other to affect the overall transport. Therefore this *non-local* nature of interfacial transport from nanoporous structures arises due to two aspects: i) inside a single pore, the interfacial flux at any given location of the interface depends on evaporation from other regions of the interface; ii) the spatial distribution of pores surrounding a single pore can also affect the net flux. Additionally, in response to different operating conditions, a change in the shape and position of the interface is

expected. The change in interfacial shape or position is a self-regulating mechanism, which affects the overall heat/mass flux from a single pore. In summary, the self-regulation of the meniscus, the non-equilibrium and non-local effects are critical aspects of phase change and transport in nanoporous structures that should be incorporated to optimize the performance of nanoporous structures for use in various industrial applications. In this study, we present a theoretical framework that addresses these effects to provide a better understanding of interfacial transport in nanopores.

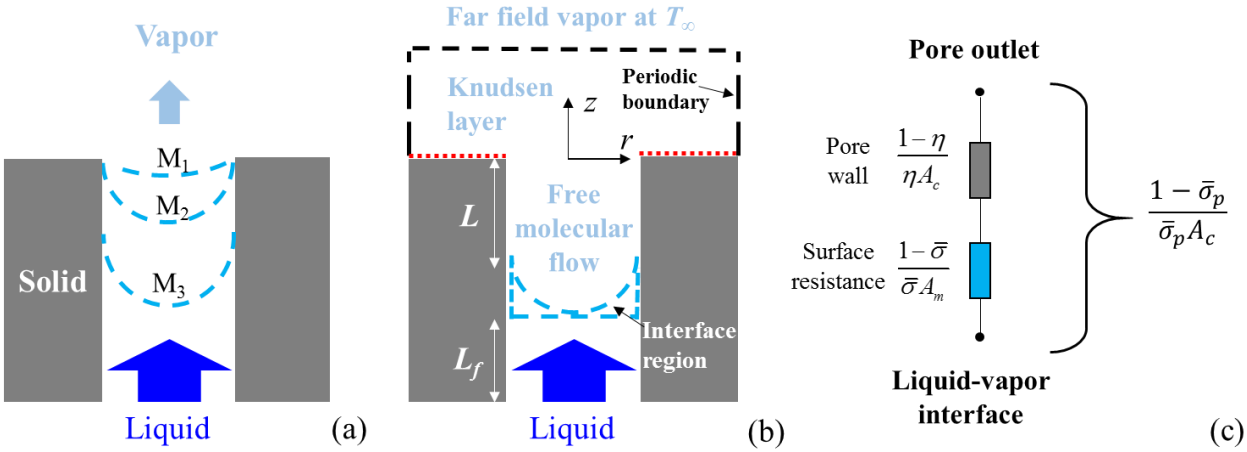

Figure 1 (a) Schematic of evaporation from a nanopore: the liquid-vapor interface can change its shape (from M_1 to M_2) or position (from M_2 to M_3) in response to different working conditions. (b) Schematic showing vapor transport from the free molecular regime inside the pore, across the Knudsen layer, to the far field equilibrium regime (c) Resistance network for the molecular transport inside the pore: the overall transport resistance in the pore is the sum of the surface resistance of the liquid-vapor interface and the geometrical resistance from the pore wall.

II. Problem Description

We examined evaporation from cylindrical nanopores (~10 - 100 nm in diameter), continuously supplied with liquid and exposed to a pure vapor ambient (Figure 1 (a)). While this configuration can be used in several applications as large-scale synthesis of nanoporous structures is now possible [23, 24, 25], it is particularly important for high flux thermal management [7, 8]. In this

arrangement, the liquid wets the pore wall and flows to the liquid-vapor interface while experiencing viscous resistance. To sustain evaporation, heat is also supplied to the interface via conduction through the liquid from the pore wall.

The liquid flow in nanopores is driven by the capillary pressure generated by the curved meniscus. Due to viscous losses in the liquid phase and the wetting nature of the pore wall, the liquid pressure at the interface is lower than the vapor pressure, and can even be negative (under tension) [8]. When the interfacial pressure difference is relatively small, the meniscus is pinned at the top of the pore (M_1 in Figure1 (a)). In this "pinning regime", the liquid-vapor interface self-regulates its curvature in response to different working conditions, which includes the pore wall temperature and liquid supply pressure. When the meniscus is fully extended and the local contact angle reaches the local receding contact angle (M_2 in Figure 1 (a)), the interface holds the maximum pressure difference. While the study of a fully extended meniscus and evaporation has been of primary interest in many studies [11, 12, 13, 14], other configurations for the meniscus are possible which need to be elucidated. As the working conditions become severe, such as higher pore wall temperatures or heat fluxes, the meniscus will recede further into the pore (M_3 in Figure 1 (a)). In this "receding regime", the fully-extended liquid-vapor interface moves within the pore to self-adjust the transport resistance in both the liquid and the vapor, and maintain the interfacial pressure difference. In more extreme operating conditions, the interface region will reach the bottom of the pore, resulting in complete dry-out.

III. Model Formulation

To predict the behavior of the interface and quantify evaporation within the pore, we have established a modeling framework for liquid and vapor transport across the pore. The interface region is defined as the liquid above the horizontal plane through the center of the meniscus (Figure

1 (b)). A uniform temperature, T, and a pressure, P_{li}, can be prescribed for the interface region due to its small scale, where spatial variations can be neglected.

A. Liquid Transport

The liquid flow from the pore inlet to the interface region is governed by the Hagen-Poiseuille equation [26]:

$$P_{in} - P_{li} = \frac{8\mu_l L_f \dot{m}}{\pi r_p^4 \rho_l} \tag{1}$$

where P_{in} is the liquid pressure at the pore inlet (the bottom of the pore), μ_l is the liquid viscosity, L_f is the flow length (Figure 1 (b)), $\dot{m}$ is the mass flow rate across the pore, r_p is the pore radius and ρ_l is the liquid density. While the liquid pressure at the interface, P_{li} is a function of P_{in} and L_f (Eqn. (1)), in this study, P_{in} is held constant and set as the saturation pressure corresponding to the far field vapor temperature, T_∞. Consequently, the effect of varying P_{li} on the overall transport is studied by varying L_f, or equivalently the pore length L_p.

B. Interfacial Pressure Balance

P_{li} is an important parameter due to its influence on the interface shape. To evaluate the shape of the liquid-vapor interface, a cylindrical coordinate system is defined in Figure 1 (b), where the origin is located at the center of the pore outlet. The interfacial pressure balance is then given by the augmented Young-Laplace equation:

$$P_{vi} - P_{li} = 2\sigma\kappa + \Pi_d \tag{2}$$

where P_{vi} is the vapor pressure on the interface, σ is the surface tension, κ is the curvature of the meniscus and Π_d is the disjoining pressure [27]. The dependence of σ on the thickness of the liquid

film is neglected in this analysis as its deviation from the bulk value was found to be within 3% for ~1 nm liquid films [28]. Note that when the liquid-vapor interface is significantly curved, there is variation of the liquid pressure inside the interface region, which is not captured in the current model (see Eqn. (1)). This nonuniformity in P_{li} can potentially affect the overall interfacial transport by varying the interface shape through Eqn. (2). However, for the analysis of evaporation in nanoporous structures, we can simplify the study as follows. Considering the liquid pressure drop in the interface region ΔP_{li}, we can rewrite Eqn. (2) while nondimensionlizing both sides with the capillary pressure of a hemispherical meniscus inside the nanopore $2\sigma/r_p$:

$$\frac{P_{vi}-P_{li}}{2\sigma/r_p}+\frac{\Delta P_{li}}{2\sigma/r_p}=\frac{\kappa}{r_p}+\frac{\Pi_d}{2\sigma/r_p} \tag{3}$$

ΔP_{li} scales with $\mu_l V_l/\delta$, where V_l is the characteristic liquid velocity. The adsorption layer thickness δ is used for the characteristic length in the interface region, which is a conservative estimation since the characteristic length for the interface region can be as large as the radius of the pore. Therefore, from this scaling argument, we obtain:

$$\frac{\Delta P_{li}}{2\sigma/r_p}\approx\frac{\mu_l V_l r_p}{2\sigma\delta} \tag{4}$$

For the chosen geometry and operating conditions, $\Delta P_{li}/(2\sigma/r_p) \ll \kappa/r_p$. Consequently, the liquid pressure drop in the interface region has an insignificant effect on Eqn. (2) and does not change the interface shape much. It is worthwhile to note that for significantly larger pore diameters (> 1 μm), this simplification is not accurate since $\Delta P_{li}/(2\sigma/r_p) \sim \kappa/r_p$. More details are provided in the supplemental.

In Eqn. (2), Π_d can be calculated from the DLVO (Derjaguin-Landau-Verwey-Overbeek) theory[27, 29, 30]:

$$\Pi_d = -\frac{A_{slv}}{6\pi(r_p - r)^3} + \Pi_{el} \tag{5}$$

where A is the Hamaker constant between the pore wall and the vapor across the liquid medium and can be obtained from the dielectric constants and refractive indices of the interacting substances [14, 27] and Π_{el} is the electrostatic component of the disjoining pressure. For non-polar fluids, $\Pi_{el} = 0$ whereas for polar fluids (*e. g.* water), it can be evaluated as [31]:

$$\Pi_{el} = \frac{\pi}{8}\left(\frac{kT}{Ze}\right)^2 \frac{1}{\left(r_p - r\right)^2} \tag{6}$$

Here, k is the Boltzmann constant, Z is the valence of ions and e is the elementary charge. While Eqn. (5) is derived for the disjoining pressure between two parallel flat surfaces, it can still be viewed as a phenomenological expression in porous geometries as supported by molecular dynamics [30]. Using the axisymmetric boundary condition at the center of the meniscus, we can integrate Eqn. (2) from $r = 0$ to $r = r_p - \delta$ to obtain the meniscus shape.

Eqns. (1) and (2), which govern the liquid transport and the interfacial pressure balance, contain unknown variables $\dot{m}$ and P_{vi}. Using mass conservation, $\dot{m}$ can be related to the vapor flux from the nanopore. However, P_{vi} does not necessarily take the equilibrium value due to the highly non-equilibrium vapor transport near the liquid-vapor interface. As a result, both $\dot{m}$ and P_{vi} have to be solved iteratively with vapor transport, which is analyzed as follows.

C. Vapor Transport

The emitted vapor molecules from the interface travel across the free molecular flow region [32] in the nanopore to the Knudsen layer outside the pore [19], and then to the far field to achieve equilibrium (Figure1 (b)). To characterize the molecular flow inside the pore, we assign an evaporation coefficient, $\bar{\sigma}_e$ and condensation coefficient, $\bar{\sigma}_c$ [33] to the liquid-vapor interface. The analysis is carried out by applying the radiation analogy [32], with $\bar{\sigma}_e$ and $\bar{\sigma}_c$ being analogous to the emissivity and absorptivity, respectively. By Kirchhoff's law, we have:

$$\bar{\sigma}_e\left(T,\mathbf{u}\right)=\bar{\sigma}_c\left(T,-\mathbf{u}\right) \tag{7}$$

where $\mathbf{u} = (u_x, u_y, u_z)$ is the velocity of a molecule leaving the interface, and the negative (−) sign indicates condensing flow. Considering the evaporating and condensing molecules, Eqn. (7) assumes that $\bar{\sigma}_e$ and $\bar{\sigma}_c$ are determined by T and u_z for any given fluid [34, 35, 36, 37]. The equality of $\bar{\sigma}_e$ and $\bar{\sigma}_c$ is well accepted during equilibrium [38]. However, even in non-equilibrium, the equality holds provided that the dependence of $\bar{\sigma}_e$ and $\bar{\sigma}_c$ on T and $\mathbf{u}$ is considered.

Eqn. (7) can be simplified by considering the effusive molecular beam experiments [39, 40], where the molecules emitted from the liquid-vapor interface do not undergo condensation, and are shown to maintain the Maxwell-Boltzmann distribution. This indicates that $\bar{\sigma}_e$ does not depend on $\mathbf{u}$. To explain this, we denote ξ as the velocity distribution function to yield the number of molecules, dn in a unit volume at a certain velocity $\mathbf{u}$, so that:

$$dn=\xi\left(\mathbf{u}\right)d^3\mathbf{u} \tag{8}$$

The equilibrium Maxwell-Boltzmann distribution ξ_M is given by:

$$\xi_M = n_{eq} \frac{\exp\left[-\mathbf{u}^2/2RT\right]}{\left(2\pi RT\right)^{3/2}} \tag{9}$$

where n_{eq} is the number density of the vapor in equilibrium with the liquid and R is the specific gas constant. The distribution of molecules emitted from the interface is then $\bar{\sigma}_e \xi_M$ [33]. The effusive molecular beam experiments show that the probability of finding a molecule at a certain velocity is the same as that for Maxwell-Boltzmann velocity distribution. Consequently:

$$\frac{\bar{\sigma}_e\left(\mathbf{u},T\right)\xi_M d^3\mathbf{u}}{\int \bar{\sigma}_e\left(\mathbf{u},T\right)\xi_M d^3\mathbf{u}} = \frac{\xi_M d^3\mathbf{u}}{\int \xi_M d^3\mathbf{u}} \tag{10}$$

which implies that $\bar{\sigma}_e$ is not a function of $\mathbf{u}$. Hence, it follows from Eqn. (7) that:

$$\bar{\sigma}_c = \bar{\sigma}_e \equiv \bar{\sigma}\left(T\right) \tag{11}$$

To determine only those vapor molecules evaporating from the interface and exiting the pore, by accounting for those molecules that recondense, the vapor transport within the pore needs to be solved. Adopting a radiative thermal transport analogy (Figure 1 (c)), we determine the "apparent emissivity", $\bar{\sigma}_p$ at the pore outlet by calculating the "surface resistance" as:

$$\frac{1-\bar{\sigma}_p}{\bar{\sigma}_p A_c} = \frac{1-\bar{\sigma}}{\bar{\sigma} A_m} + \frac{1-\eta}{\eta A_c} \tag{12}$$

Here, A_c is the cross-section area of the pore, A_m is the total surface area of the meniscus, which can be determined from Eqn. (2), and η is the molecule transmission probability from the interface to the pore outlet. The overall molecular transport resistance consists of a surface resistance from the meniscus and a geometrical resistance from the pore wall. The pore wall can be considered as an intermediate emitter/absorber with area A_c and emissivity η. The transmission probability η is

calculated as a function of the reduced transport length L^*, defined as L/r_p, where L is the distance between the top of the meniscus and the pore outlet, as shown in Figure 1 (b) [41]:

$$\eta = 1 + \frac{L^{*2}}{4} - \frac{L^*}{4}\sqrt{L^{*2}+4} - \frac{\left[\left(8 - L^{*2}\right)\sqrt{L^{*2}+4} + L^{*3} - 16\right]^2}{72L^*\sqrt{L^{*2}+4} - 288\ln\left(\frac{L^* + \sqrt{L^{*2}+4}}{2}\right)} \tag{13}$$

Note that in the pinning case, $L^* = 0$, $\eta = 1$ and Eqn. (12) simply accounts for the self-condensation effect of the curved interface. The calculation of $\bar{\sigma}_p$ allows modeling evaporation from the pore outlet to analyze vapor transport across the Knudsen layer to the far field.

A moment method was established [19] to solve the half-space evaporation problem, with a far field boundary at $z \to \infty$, and an evaporative boundary at $z = 0$, which has shown good agreement with numerical solutions of the Boltzmann transport equations (BTE) [17, 18]. This agreement ensures that when the meniscus is pinned at the top of the pore and not significantly curved, the free molecular transport inside the pore does not play a significant role, and our model predictions match the results from BTE. The moment method allows conserving mass, momentum and energy, as opposed to the traditional Schrage equation used in previous studies, which considers only mass conservation [17]. In this study, we apply the moment method to solve the vapor transport outside the pore, as described below.

Assuming an ideal gas behavior in the vapor phase, we have:

$$n_{eq} / P_{v,eq} = n_{v,sat} / P_{sat} \tag{14}$$

where $P_{v,eq}$ is the equilibrium vapor pressure, P_{sat} is the saturation pressure, and $n_{v,sat}$ is the number density of molecules in the saturated vapor at T. $P_{v,eq}$ is calculated by matching the liquid and vapor interfacial chemical potential [42]:

$$\frac{P_{li}-P_{sat}}{\rho_l}=RT\ln\left(\frac{P_{v,eq}}{P_{sat}}\right) \tag{15}$$

The conservation of molecules at the pore outlet requires:

$$\xi\,|_{z=0,u_z>0,r<r_p}=\bar{\sigma}_{\mathrm{p}}\xi_M+\left(1-\bar{\sigma}_{\mathrm{p}}\right)\xi\,|_{z=0,u_z<0,r<r_p} \tag{16}$$

Eqn. (14) implies that the molecules leaving the pore consist of two parts, namely the emitted molecules, $\bar{\sigma}_p\xi_M$ and the reflected molecules, $(1-\bar{\sigma}_p)\,\xi\,|_{z=0,\,u_z<0,\,r<r_p}$. In equilibrium, we have:

$$\xi^{eq}\,|_{z=0,u_z>0,r<r_p}=\xi^{eq}\,|_{z=0,u_z<0,r<r_p}=\xi_M \tag{17}$$

which automatically satisfies Eqn. (16). In non-equilibrium, the distribution in the condensing flow is assumed to take the following form [19]:

$$\xi\,|_{z=0,u_z<0,r<r_p}=n_c\,\frac{\exp\left[-\left(\mathbf{u}-u_\infty\hat{\mathbf{z}}\right)^2\Big/\left(2RT_\infty\right)\right]}{\left(2\pi RT_\infty\right)^{3/2}} \tag{18}$$

where $\hat{\mathbf{z}}$ is the unit vector in z-direction, and n_c (a parameter yet to be calculated) denotes the effective number density of vapor molecules at *z=0*, directed back to the pore outlet. Note that on the top surface of the pore wall (shown as the red dotted line in Figure 1 (b)), there is no flux in the *z*-direction. Since the gradient of the flux is also zero, it follows from mass conservation that there cannot be any flux in the r-direction either, which requires the pressure on the top surface of the pore wall (P_w) to satisfy the following equation,

$$P_w=m\int\xi\,|_{z=0,r<r_p}\left(\mathbf{u}\cdot\hat{\mathbf{r}}\right)^2 d^3\mathbf{u} \tag{19}$$

where *m* is the molecular mass and $\hat{\mathbf{r}}$ is the unit vector in r-direction. In the far field, where thermodynamic equilibrium is again realized,

$$\xi|_{z\to\infty} = n_\infty \frac{\exp\left[-\left(\mathbf{u}-u_\infty\hat{\mathbf{z}}\right)^2 / 2RT_\infty\right]}{\left(2\pi RT_\infty\right)^{3/2}} \tag{20}$$

where u_∞ is the bulk velocity of the far field vapor. By conserving mass, momentum and energy ($\dot{m}$, F_z and $\dot{E}$) between the pore outlet and the far field within the periodic boundaries of the unit cell (Figure 1 (b)), we have:

$$\dot{m} = mA_c \int \xi|_{z=0}\, u_z d^3\mathbf{u} = mA_u \int \xi|_{z\to\infty}\, u_z d^3\mathbf{u} \tag{21}$$

$$F_z = \left(A_u - A_c\right)P_w + mA_c \int \xi|_{z=0}\, u_z^2 d^3\mathbf{u} = mA_u \int \xi|_{z\to\infty}\, d^3\mathbf{u} \tag{22}$$

$$\dot{E} = mA_c \int \xi|_{z=0}\, u_z \frac{\mathbf{u}^2}{2} d^3\mathbf{u} = mA_u \int \xi|_{z\to\infty}\, u_z \frac{\mathbf{u}^2}{2} d^3\mathbf{u} \tag{23}$$

respectively, where A_u is the total area of one unit cell. Note that Eqn. (21), (22) and (23) contain $\bar{\sigma}_p$, which depends on P_{vi} (Eqns. (2) and (12)). To evaluate P_{vi}, we need the velocity distribution function at z = -L, which is obtained as follows. The fraction of the overall condensing flow reaching z = -L from the pore outlet is given by:

$$\xi|_{z=-L,u_z<0} = \eta\xi|_{z=0,u_z<0} \tag{24}$$

where η is calculated using Eqn. (8). Conserving the number of molecules at z = -L, we have:

$$\xi|_{z=-L,u_z>0} = \bar{\sigma}_1\xi_M + \left(1-\bar{\sigma}_1\right)\xi|_{z=-L,u_z<0} \tag{25}$$

where $\bar{\sigma}_1$ is the apparent emissivity at z = -L, which, by the invariance of surface resistance, satisfies:

$$\frac{1-\bar{\sigma}_1}{\bar{\sigma}_1 A_c} = \frac{1-\bar{\sigma}}{\bar{\sigma} A_m} \tag{26}$$

The average number density, n_1 at z = -L is then given by:

$$n_1 = \int \xi_{z=-L} d^3\mathbf{u} \tag{27}$$

The bulk vapor velocity, u_1 can then be calculated from mass conservation as:

$$mn_1 u_1 A_c = \dot{m} \tag{28}$$

Balancing the momentum in the z-direction between $z = -L$ and $z = 0$ gives P_{vi} as follows:

$$P_{vi} + mn_1 u_1^{\,2} = m\int \xi\,|_{z=0}\; u_z^{\,2} d^3\mathbf{u} \tag{29}$$

By iteratively solving the liquid transport, the interfacial pressure balance and the vapor transport (see the supplemental), we can determine the evaporation regime (pinning or receding) and the net heat/mass flux from a single nanopore.

IV. Results and Discussion

To illustrate the utility of the new theoretical framework, a case study was carried out considering evaporation of octane from silicon nanopores into a vapor ambient maintained at T_∞ = 300 K. While the modelling framework can be applied to a wide range of working fluids, octane was chosen here due to its relatively large mean free path ($\lambda \sim 1.1$ μm [43] at the working condition) as we require $\lambda \gg r_p$ to result in a free molecular flow in the nanopore [32]. In this study, the thermophysical properties of octane were obtained as a function of temperature[44, 45, 46] and the results are presented in terms of dimensionless quantities defined in Table 1. For reference, we set the evaporation and condensation coefficients as $\bar{\sigma} = 1$, the pore radius r_p = 40 nm, the pore length L_p = 10 μm, and the porosity ϕ = 0.2 and the receding contact gale θ_r = 0 °.

Table 1 Non-dimensional quantities used in the present analysis and their physical meaning ($n_{\mathrm{sat},\infty}$ denotes the number density of saturated vapor at T_∞).

Symbol	Expression	*Physical* meaning
T^*	$(T - T_\infty)/T_\infty$	Superheat
j^*	$\frac{n_\infty u_\infty}{\phi n_{\text{sat},\infty}\sqrt{5/3 \cdot RT_\infty}}$	Heat/mass flux over one pore
h^*	j^*/T^*	Heat transfer coefficient
r^*	r/r_p	r-coordinate
z^*	z/r_p	z-coordinate
L^*	L/r_p	Transport length

In Figure 2 (a), the dimensionless heat/mass flux j^* and heat transfer coefficient (HTC) h^* normalized over the cross-section area of the pore are shown as a function of the dimensionless superheat T^*. When T^* is relatively low, evaporation occurs in the pinning regime, where both the flux and the HTC increase as the temperature rises due to a higher intensity of molecular emission. As the superheat increases, the meniscus extends further (Figure 2(b)) until it becomes fully extended. Subsequently, the meniscus will start to recede into the pore. In this receding regime, as the superheat is enhanced further, the receding length increases and with the meniscus further inside the pore, there is a lower probability for the vapor molecules to escape from the pore (Figure 2 (c)). Consequently, the increase in flux is less steep and the HTC decreases in the receding regime. When the receding length equals the total pore length, the meniscus reaches the bottom of the pore and the vapor expands into the liquid causing complete dry-out, an undesirable phenomenon for applications relying on maximizing the rate of evaporation. The interfacial transport is more efficient in the pinning regime than the receding regime due to minimal vapor transport resistance.

Therefore, to achieve the highest possible fluxes with relative low superheats, it is more favorable to keep the liquid-vapor interface pinned at the top of the pore. This framework identifies the transition from the pinning to receding mode of evaporation in nanopores.

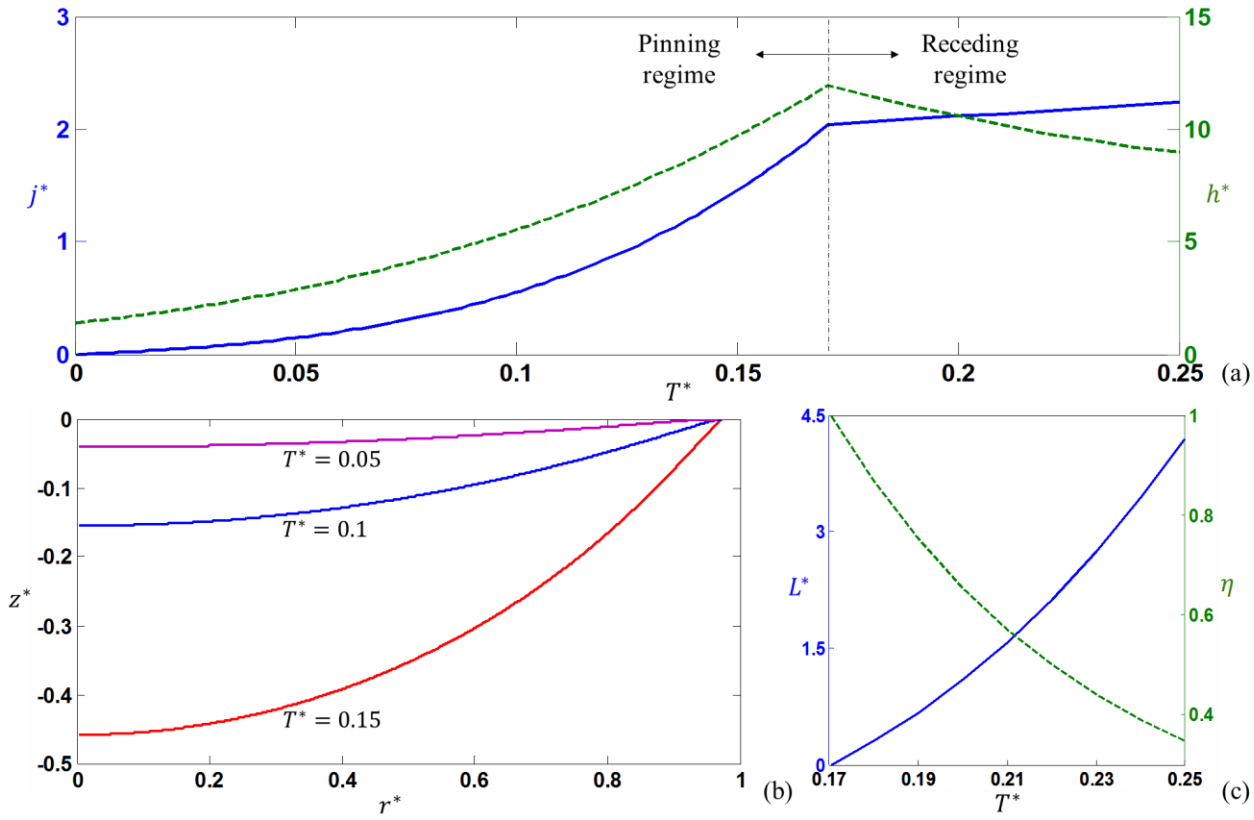

Figure 2 (a) Dimensionless flux j^* (blue solid line) and heat transfer coefficient h^* (green dash line) *vs.* dimensionless superheat T^* for the reference case (with the evaporation coefficient fixed at 1, the pore radius at 40 nm and the pore length at 10 μm) (b) Shape of liquid-vapor interface for selected superheats in the pinning regime (c) Dimensionless receding length L^* (blue solid line) and transmission probability η (green dash line) *vs.* dimensionless superheat T^* in the receding regime

We also studied the effect of different geometric parameters on the regime transition and interfacial flux. In Figure 3 (a) and (b), r_p and L_p were varied from the reference case, and the corresponding j^* *vs.* T^* are shown for comparison. In Figure 3 (a), as the pore radius decreases, the capillary pressure (~ $1/r_p$) supporting the flow in the nanopore increases. However, the viscous loss inside the pore (~ $1/r_p^2$ for a fixed flux) increases faster, which gives rise to an earlier regime transition.

On the other hand, in Figure 3 (b), the regime transition, namely recession of the meniscus can also occur at much lower superheats when longer pores are utilized because it increases the viscous losses in the liquid flow.

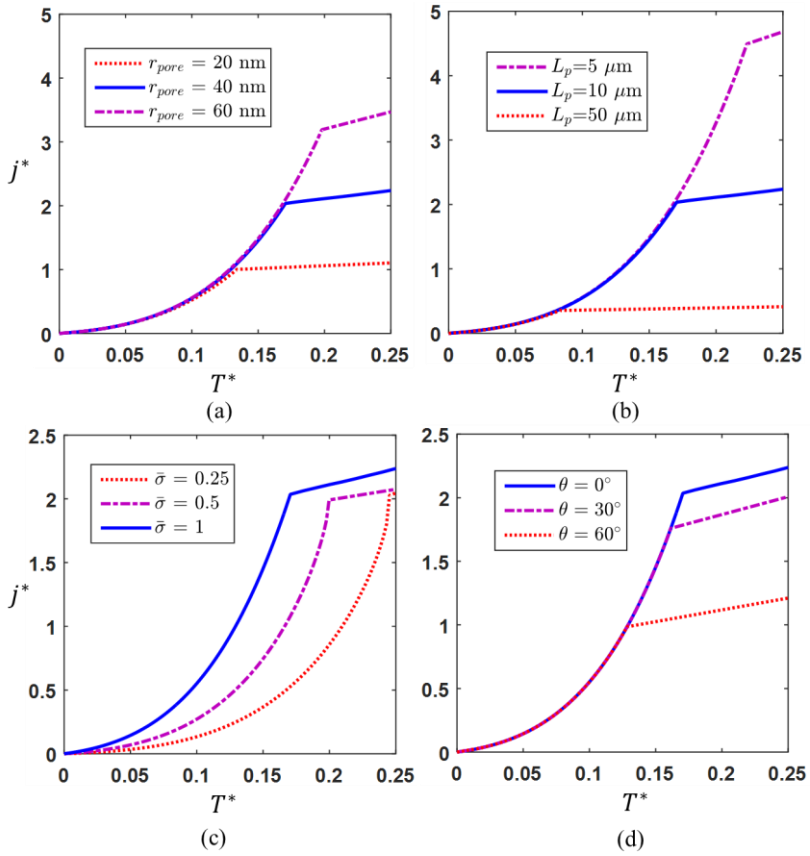

Figure 3 Effect of (a) pore radius, (b) pore length, (c) evaporation coefficient and (d) receding contact angle on the interfacial transport: r_p, L_p, $\bar{\sigma}$ and θ_r were independently varied and the corresponding j^* as a function of T^* plots are compared to the reference case where the parameters are set as: r_p = 40 nm, L_p = 10 μm, $\bar{\sigma}$ = 1, θ_r = 0 ° and ϕ = 0.2.

It should be noted that evaporation of thin liquid films has been analyzed significantly via both experiments and computational modeling in literature. While the theoretical framework developed in this study is more consistent for the chosen geometry and operating conditions, it does not allow a direct comparison with previous studies that consider significantly different operational and

geometric parameters. Furthermore, the evaporation coefficient at the interface ($\bar{\sigma}$) and the receding contact angle on the pore wall (θ_r) can also affect the overall rate of evaporation from nanopores. An accurate knowledge of these parameters is necessary to predict the overall performance. Consequently, apart from studying sensitivity to the geometric parameters, we also quantify the effect of $\bar{\sigma}$ and θ_r. In Figure 3 (c), for a given superheat, a smaller $\bar{\sigma}$ corresponds to higher vapor transport resistance and lower interfacial flux, resulting in less viscous loss in the liquid phase. Consequently, recession begins at a higher superheat. On the other hand, in Figure 3 (d) when the liquid is less wetting (θ_r is relatively large), the interfacial transport behaves exactly the same as the perfect wetting case except that the meniscus recedes at a lower superheat.

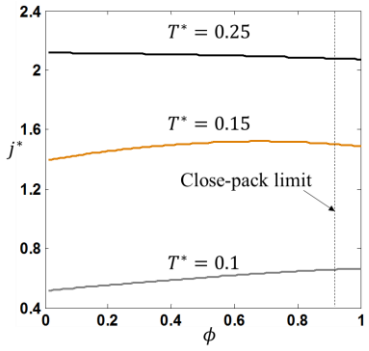

Figure 4 Effect of porosity ϕ on the interfacial transport from one single pore for select superheats with other parameters the same as in the reference case (r_p = 40 nm, L_p = 10 μm, $\bar{\sigma}$ = 1 and θ_r = 0 °)

To study the effect of the spatial distribution of pores, the interfacial flux is plotted as a function of the porosity for select superheats (Figure 4). In general, the porosity, which is not determined by a single pore, *i.e.*, a global parameter, does not influence the interfacial transport over one single pore significantly. However, the net flux shows a different trend with porosity at different temperatures. We attribute this to the interaction of vapor emerging from a single pore with two other sources of vapor flow, namely the molecules directed back at the interface from the vapor ambient (which has a distribution function of $\xi \mid_{z \to \infty,\, u_z < 0}$), and the vapor emitted from the

neighboring pores. When the superheat is relatively low, the vapor flow from the ambient is significant. Hence, a higher porosity ensures that for each unit cell, there are fewer molecules directed back at the liquid-vapor interface, which favors higher evaporation. When the superheat is relatively high, the vapor flow emitted by neighboring pores is more important. Consequently, lower porosities result in better pore-level transport since the interactions with the neighboring pores are lowered. For an intermediate superheat where the two effects are comparable, there is an optimum porosity to ensure maximum flux from a single pore. Note that the planar close-pack limit is $\phi \approx 0.907$, so any porosity beyond that cannot be achieved in practice.

The accuracy of this model to predict the interfacial flux and the regime transition depends on several factors including the evaporation coefficient and the receding contact angle. While the receding contact angle depends on the selection of the working fluid and pore wall material, it also depends on the roughness of the pore wall, which requires detailed experimental characterization. Similarly, while the evaporation and condensation coefficients have been determined using molecular dynamics study, a significant disagreement still exists between modeling and experimental findings[33]. Consequently, careful experimental characterization of evaporation coefficient is necessary. With the limited experimental studies on evaporation from nanostructures in literature, comparison of existing results to that from our theoretical framework is challenging. In the future, we aim to perform detailed experimental investigations of high flux evaporation from nanopores to validate the details of our model.

V. Conclusions

The modeling framework presented in this study offers a fundamental understanding of evaporation at small scales (~10 – 100 nm), which has significance in thermal management of electronics and water purification. The model elucidates the self-regulating nature of evaporation

in nanoporous structures and predicts the overall transport to occur either in a pinned or receding regime. The model suggests a more efficient transport of energy in the pinning regime, and is capable of identifying conditions that can lead to a regime transition. The model also incorporates the non-equilibrium effects due to higher heat/mass flux, and the non-local effects due to the use of nanoporous geometries. Consequently, a more consistent and thorough understanding of evaporation at small scales is developed in this study. In order to illustrate how this model can be applied to predict phase change, effects of geometric parameters on octane evaporating in silicon nanopores were studied to provide guidelines for the design and fabrication of micro/nanostructured surfaces, and to determine conditions suitable for maximizing the energy transport. While our modeling framework was developed to emulate the underlying physics more consistently, the accuracy of this model to predict the interfacial flux and the regime transition, depends on the evaporation and condensation coefficients and the receding contact angle. Further investigation into these two microscopic parameters is necessary to gain a comprehensive understanding of the interfacial transport at small scales.

Acknowledgements

This work is supported by the DARPA ICECool Fundamentals program with Dr. Avram Bar-Cohen as the program manager.

References

1. Rand, R. H. Fluid mechanics of green plants. *Annual Review of Fluid Mechanics* **1983,** *15*, 29-45.
2. Mosher, H. Simultaneous study of constituents of urine and perspiration. *J. biol. Chem* **1933,** *99*, 781-790.
3. Narayanan, S.; Fedorov, A. G.; Joshi, Y. K. Gas-assisted thin-film evaporation from confined spaces for dissipation of high heat fluxes. *Nanoscale Microscale Thermophys. Eng.* **2009,** *13*, 30-53.
4. Cai, Q.; Chen, C.-L. Design and test of carbon nanotube biwick structure for high-heat-flux phase change heat transfer. *J. Heat Transfer* **2010,** *132*, 052403.
5. Nam, Y.; Sharratt, S.; Cha, G.; Ju, Y. S. Characterization and modeling of the heat transfer performance of nanostructured Cu micropost wicks. *J. Heat Transfer* **2011,** *133*, 101502.
6. Ćoso, D.; Srinivasan, V.; Lu, M.-C.; Chang, J.-Y.; Majumdar, A. Enhanced heat transfer in biporous wicks in the thin liquid film evaporation and boiling regimes. *J. Heat Transfer* **2012,** *134*, 101501.
7. Hanks, D. F.; Lu, Z.; Narayanan, S.; Bagnall, K. R.; Raj, R.; Xiao, R.; Enright, R.; Wang, E. N. In *Nanoporous evaporative device for advanced electronics thermal management*, Thermal and Thermomechanical Phenomena in Electronic Systems (ITherm), 2014 IEEE Intersociety Conference on, 2014; IEEE, pp 290-295.
8. Xiao, R.; Maroo, S. C.; Wang, E. N. Negative pressures in nanoporous membranes for thin film evaporation. *Appl. Phys. Lett.* **2013,** *102*, 123103.
9. Humplik, T.; Lee, J.; O'Hern, S.; Fellman, B.; Baig, M.; Hassan, S.; Atieh, M.; Rahman, F.; Laoui, T.; Karnik, R. Nanostructured materials for water desalination. *Nanotechnology* **2011,** *22*, 292001.
10. Lee, J.; Laoui, T.; Karnik, R. Nanofluidic transport governed by the liquid/vapour interface. *Nat. Nanotechnol.* **2014,** *9*, 317-323.
11. Wayner Jr, P.; Kao, Y.; LaCroix, L. The interline heat-transfer coefficient of an evaporating wetting film. *Int. J. Heat Mass Transfer* **1976,** *19*, 487-492.
12. Swanson, L.; Herdt, G. Model of the evaporating meniscus in a capillary tube. *J. Heat Transfer* **1992,** *114*, 434-441.
13. Wang, H.; Garimella, S. V.; Murthy, J. Y. Characteristics of an evaporating thin film in a microchannel. *Int. J. Heat Mass Transfer* **2007,** *50*, 3933-3942.
14. Narayanan, S.; Fedorov, A. G.; Joshi, Y. K. Interfacial Transport of Evaporating Water Confined in Nanopores. *Langmuir* **2011,** *27*, 10666-10676.
15. Derjaguin, B.; Churaev, N.; Muller, V. Wetting films. In *Surface Forces*; Springer, 1987, pp 327-367.
16. Schrage, R. W. *A theoretical study of interphase mass transfer*; Columbia University Press1953.
17. Avdeev, A. A.; Zudin, Y. B. Kinetic analysis of intensive evaporation (method of reverse balances). *High Temp.* **2012,** *50*, 527-535.
18. Rose, J. W. Accurate approximate equations for intensive sub-sonic evaporation. *Int. J. Heat Mass Transfer* **2000,** *43*, 3869-3875.
19. Labuntsov, D.; Kryukov, A. Analysis of intensive evaporation and condensation. *Int. J. Heat Mass Transfer* **1979,** *22*, 989-1002.

20. Sone, Y.; Takata, S.; Golse, F. o. Notes on the boundary conditions for fluid-dynamic equations on the interface of a gas and its condensed phase. *Phys. Fluids* **2001,** *13*, 324.
21. Karniadakis, G.; Beskok, A.; Gad-el-Hak, M. Micro flows: fundamentals and simulation. *Appl. Mech. Rev.* **2002,** *55*, 76.
22. Imdakm, A.; Khayet, M.; Matsuura, T. A Monte Carlo simulation model for vacuum membrane distillation process. *J. Membr. Sci.* **2007,** *306*, 341-348.
23. Wang, Y.; Wei, F.; Luo, G.; Yu, H.; Gu, G. The large-scale production of carbon nanotubes in a nano-agglomerate fluidized-bed reactor. *Chem. Phys. Lett.* **2002,** *364*, 568-572.
24. Guo, L. J. Nanoimprint lithography: methods and material requirements. *Adv. Mater.* **2007,** *19*, 495-513.
25. Lee, W.; Ji, R.; Ross, C. A.; Gösele, U.; Nielsch, K. Wafer‐Scale Ni Imprint Stamps for Porous Alumina Membranes Based on Interference Lithography. *Small* **2006,** *2*, 978-982.
26. Kundu, P.; Cohen, I. Fluid mechanics. 2004. Elsevier Academic Press, 2008.
27. Israelachvili, J. N. *Intermolecular and surface forces: revised third edition*; Academic press2011.
28. Matsuoka, H.; Oka, K.; Yamashita, Y.; Saeki, F.; Fukui, S. Deformation characteristics of ultra-thin liquid film considering temperature and film thickness dependence of surface tension. *Microsyst. Technol.* **2011,** *17*, 983-990.
29. Hu, H.; Weinberger, C. R.; Sun, Y. Effect of Nanostructures on the Meniscus Shape and Disjoining Pressure of Ultrathin Liquid Film. *Nano Lett.* **2014,** *14*, 7131-7137.
30. Hu, H.; Sun, Y. Molecular dynamics simulations of disjoining pressure effect in ultra-thin water film on a metal surface. *Appl. Phys. Lett.* **2013,** *103*, 263110.
31. Derjaguin, B.; Churaev, N. Structural component of disjoining pressure. *J. Colloid Interface Sci.* **1974,** *49*, 249-255.
32. Lee, J.; Karnik, R. Desalination of water by vapor-phase transport through hydrophobic nanopores. *J. Appl. Phys.* **2010,** *108*, 044315.
33. Marek, R.; Straub, J. Analysis of the evaporation coefficient and the condensation coefficient of water. *Int. J. Heat Mass Transfer* **2001,** *44*, 39-53.
34. Bond, M.; Struchtrup, H. Mean evaporation and condensation coefficients based on energy dependent condensation probability. *Physical Review E* **2004,** *70*, 061605.
35. Nagayama, G.; Tsuruta, T. A general expression for the condensation coefficient based on transition state theory and molecular dynamics simulation. *The Journal of Chemical Physics* **2003,** *118*, 1392-1399.
36. Tsuruta, T.; Nagayama, G. Molecular dynamics studies on the condensation coefficient of water. *The Journal of Physical Chemistry B* **2004,** *108*, 1736-1743.
37. Tsuruta, T.; Tanaka, H.; Masuoka, T. Condensation/evaporation coefficient and velocity distributions at liquid–vapor interface. *Int. J. Heat Mass Transfer* **1999,** *42*, 4107-4116.
38. Carey, V. P. Liquid-vapor phase-change phenomena. **1992**.
39. Faubel, M.; Schlemmer, S.; Toennies, J. A molecular beam study of the evaporation of water from a liquid jet. *Zeitschrift für Physik D Atoms, Molecules and Clusters* **1988,** *10*, 269-277.
40. Johnson, T. H. The Production and Measurement of Molecular Beams. *Physical Review* **1928,** *31*, 103.
41. Berman, A. Free molecule transmission probabilities. *J. Appl. Phys.* **1965,** *36*, 3356-3356.
42. Faghri, A. *Heat pipe science and technology*; Global Digital Press1995.
43. Grad, H. On the kinetic theory of rarefied gases. *Commun. Pure Appl. Math.* **1949,** *2*, 331-407.

44. Span, R.; Wagner, W. Equations of state for technical applications. II. Results for nonpolar fluids. *Int. J. Thermophys.* **2003,** *24*, 41-109.
45. Liley, P. E.; Makita, T.; Tanaka, Y. *Properties of inorganic and organic fluids*; Taylor & Francis1988; Vol. 1.
46. Somayajulu, G. A generalized equation for surface tension from the triple point to the critical point. *Int. J. Thermophys.* **1988,** *9*, 559-566.

TOC Graphic

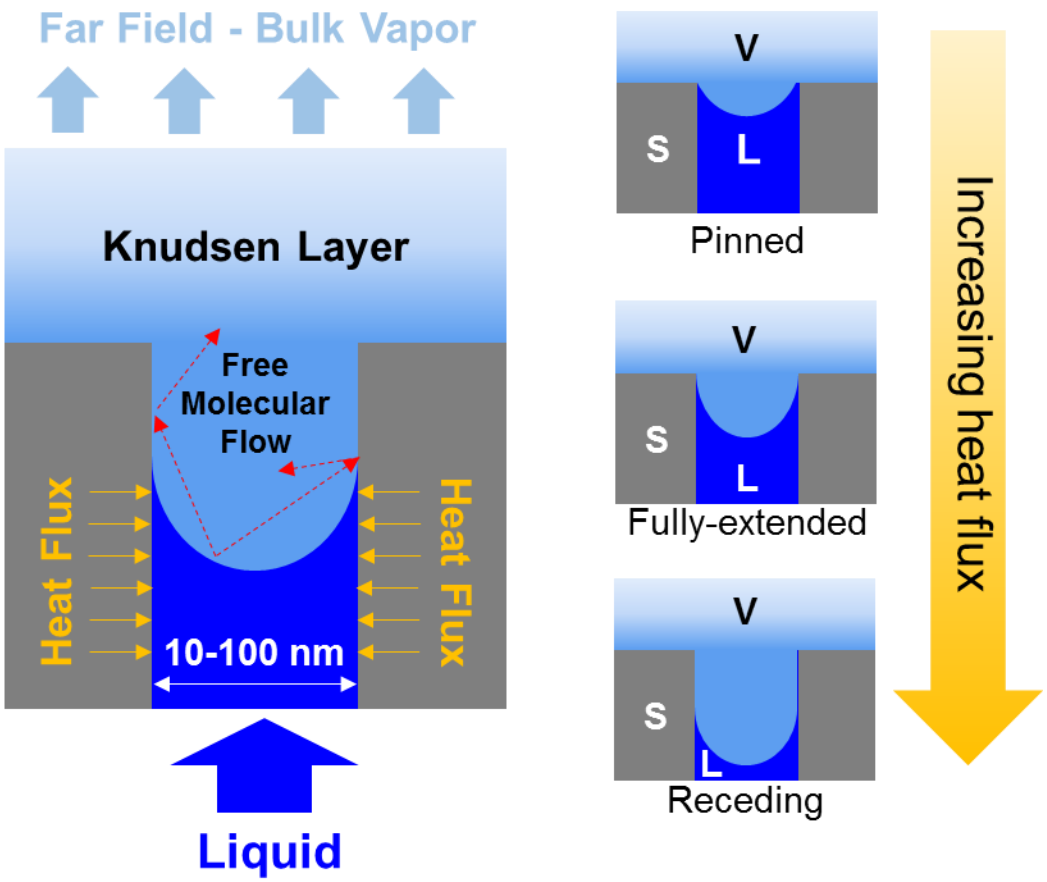
Far Field - Bulk Vapor
Knudsen Layer
Free
Molecular
Flow
Heat Flux
Heat Flux
10-100 nm
Liquid
V
S
L
Pinned
V
S
L
Fully-extended
V
S
L
Receding
Increasing heat flux

Supplemental Information

Modeling of evaporation from nanopores with non-equilibrium and non-local effects

Zhengmao Lu, Shankar Narayanan and Evelyn N. Wang*

Department of Mechanical Engineering, Massachusetts Institute of Technology, Cambridge, Massachusetts 02139, USA

I. Overall Computation Strategy

We describe the overall computation strategy where Fig. S1 shows a flow chart for the computations performed. The computation is initialized with the liquid pressure of the interface region P_{li} set as the pore inlet pressure P_{en} and the vapor pressure acting on the meniscus P_{vi} set as the saturation pressure in the far field vapor. With Eqn. (2) (all the equation numbers here are referred to the ones in the main text), the interface shape can be solved for and the working regime is also determined. In the pinning regime, the apparent evaporation coefficient $\bar{\sigma}_{\mathrm{p}}$ at the pore outlet can then be calculated from Eqn. (12) and P_{vi} can be obtained through Eqn. (14) – (27). If P_{vi} converges to its previous value, the mass flow rate can be extracted from the vapor transport and plugged into the liquid transport (Eqn. (1)) to result in P_{li}. If P_{li} converges to its previous value as well, the problem is then solved in the pinning regime. If either P_{li} or P_{vi} does not meet the convergence criteria (defined as the relative change less than 0.01%), more iterations are conducted. In the receding regime, the meniscus is considered as fully extended. Hence, the

* To whom correspondence should be addressed: enwang@mit.edu

interfacial pressure difference (P_{vi} - P_{li}) is known given a working condition. We can calculate the receding length L from the liquid transport and the vapor transport, respectively, and matching them allows us to iteratively obtain L and subsequently solve for the interfacial transport in the receding regime.

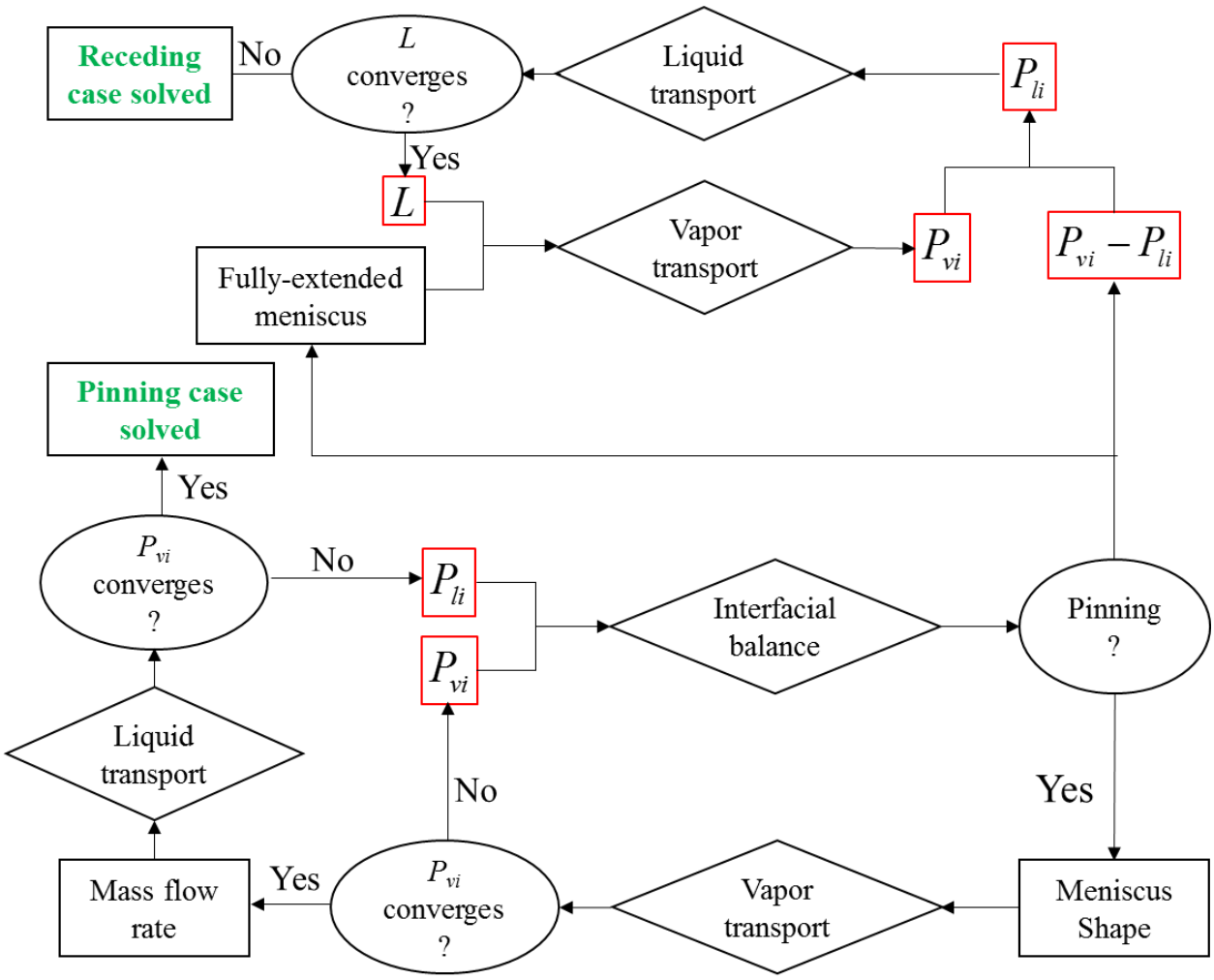

Fig. S1 Computation flow chart describing the iteration loop to determine the evaporative flux across the nanopores.

II. Nonuniformity in Liquid Pressure of Interface Region

The nonuniformity in the liquid pressure of the interface region can potentially affect the overall interfacial transport by varying the interface shape through Eqn. (2). The significance of the liquid pressure variation at the interface can be estimated using Eqn. (4). With a relatively high heat flux ($\dot{q}''$ = 1 kW/cm^2), the characteristic fluid velocity in the pore can be calculated as:

$$V_l = \frac{\dot{q}''}{\rho_l h_{fg}} \tag{S1}$$

Using saturated liquid properties of octane at 300 K, ρ_l = 696 kg/m^3 and h_{fg} = 363.3 kJ/kg, which results in V_l = 3.95 × 10^{-2} m/s. With r_p = 40 nm, δ = 1 nm, and σ = 20.98 mN/m, μ_l = 582.1 μPa·s, determined at 300 K, $\Delta P_{li}/(2\sigma/r_p)$ ~ 0.02 and κ/r_p is ~ 1 in Eqn.(3). Therefore, $\Delta P_{li}/(2\sigma/r_p)$ can be neglected and the nonuniformity in the liquid pressure has a negligible effect on the interfacial transport for the cases studied in this work. However, it is clear that for significantly larger pore diameters (> 1μm), $\Delta P_{li}/(2\sigma/r_p)$ becomes greater than 0.25. Consequently, $\Delta P_{li}/(2\sigma/r_p)$ cannot be neglected.